Vibration Sensing in Smart Machine Rotors using Internal MEMS Accelerometers

Samuel Jiménez[a,*], Matthew O. T. Cole[a,1], Patrick S. Keogh[a]

[a] *Department of Mechanical Engineering, University of Bath, Claverton Down, Bath, BA2 7AY, United Kingdom*

Abstract

This paper presents a novel topology for enhanced vibration sensing in which wireless MEMS accelerometers embedded within a hollow rotor measure vibration in a synchronously rotating frame of reference. Theoretical relations between rotor-embedded accelerometer signals and the vibration of the rotor in an inertial reference frame are derived. It is thereby shown that functionality as a virtual stator-mounted displacement transducer can be achieved through appropriate signal processing. Experimental tests on a prototype rotor confirm that both magnitude and phase information of synchronous vibration can be measured directly without additional stator-mounted key-phasor sensors. Displacement amplitudes calculated from accelerometer signals will become erroneous at low rotational speeds due to accelerometer zero-g offsets, hence a corrective procedure is introduced. Impact tests are also undertaken to examine the ability of the internal accelerometers to measure transient vibration. A further capability is demonstrated, whereby the accelerometer signals are used to measure rotational speed of the rotor by analysing the signal component due to gravity. The study highlights the extended functionality afforded by internal accelerometers and demonstrates the feasibility of internal sensor topologies, which can provide improved observability of rotor vibration at externally inaccessible rotor locations.

Keywords: rotordynamics, accelerometers, rotor-mounted sensors, smart machine rotor

1. Introduction

Sensing and control of rotor vibration can provide useful functionality in the operation of rotating machinery. Significant advances have been made in recent years in signal processing and active control technology, which have allowed improvements in condition monitoring and vibration

[*] Corresponding author

Email addresses: s.jimenez@bath.ac.uk (Samuel Jiménez), motcole@hotmail.com (Matthew O. T. Cole), p.s.keogh@bath.ac.uk (Patrick S. Keogh)

[1] Present address: Faculty of Engineering, Chiang Mai University, 239 Huay Kaew Rd., Muang District, Chiang Mai, Thailand 50200

reduction capability [1]. Further benefits may be derived from increased operating speed range, power density and reliability. From the perspective of active vibration control, this translates into demands for improved observability and controllability of vibration phenomena.

Conventional systems typically rely on eddy current sensors to obtain rotor displacement data, while vibration control can be achieved through the use of active magnetic bearings (AMBs) [2]. These components are stator-mounted, with the rotor being a passive element. Consequently, the outer surface of the rotor is shared between active components (sensors and actuators) and working surfaces (impellers, permanent magnets, seals, etc.). This brings three constraints:

(a) Limited multiplicity of sensors and actuators
(b) Limited freedom in positioning of sensors and actuators
(c) Sensors and actuators are exposed to the working environment

These constraints ultimately limit the capability of stator-mounted active system designs. Thus, alternative sensing and actuation topologies which can overcome these constraints are sought, so that the desired improvements in performance may be achieved.

In this paper a new rotor topology involving wireless sensors located inside the rotating shaft is proposed. The inner core of a rotor contributes little to the overall bending stiffness and is hence an ideal space in which to place components. Such a topology would allow a greater number of sensors and actuators to be used when compared against conventional stator-mounted arrangements, as the presence of working surfaces would not interfere with the location of the active components. Crucially, this would also enable their position to be chosen for improved observability and controllability. For example, sensors could be located in the same plane as a critical sealing ring, or an actuator could be placed at an antinode for maximum controllability. Furthermore, locating components within the shaft protects them from harsh environments. Internal sensor topologies may also offer other advantages when compared against specific sensing technologies. For instance, eddy current displacement probes are sensitive to the rotor material and geometry, as well as the properties of the gap fluid [3]. Similarly, optical techniques such as Laser Doppler Vibrometry may suffer from speckle noise arising from rough surfaces [4]. However, internally located sensors do not require interaction with the rotor surface and are hence not affected by the rotor material or its surface finish.

The use of a rotor-mounted actuator for an active vibration control system was investigated by Van de Vegte [3], who used a mass-balancing device fixed on a rotating shaft. Gosiewski [4] presented an evolution of the idea by automating the control using a computer, while Lee and Kim [5] developed a wireless transmission system to provide control signals for actuation.

In the case of sensors, however, stator-mounted devices have been used almost exclusively. Typically, these are bearing mounted accelerometers [6] or eddy current displacement sensors [7–10]. Christensen and Santos [11] have used blade-mounted strain gauges as part of an experimental vibration control system. For qualification testing in the aerospace industry, Knappett and Garcia [12] provide an example of instrumentation of compressor blades with strain gauges to infer stress conditions. Sloetjes and de Boer [13] used strain gauges bonded to the surface of a rotor to measure bending of the shaft, although performance limitations were encountered.

In recent years the evolution of electronics has led to compact and robust MEMS sensors becoming commercially available. MEMS accelerometers have attracted interest for rotor-mounted sensor applications. Wireless accelerometer systems have been used by Arebi *et al.* [14] to detect misalignment of rotating coupled shafts, and have been shown to perform better than some established sensing technologies [15]. Baghli *et al.* [16] used them to measure the instantaneous torque produced by an induction motor coupled to a shaft. Elnady *et al.* [17] showed that rotor-mounted MEMS accelerometers can detect basic rotor dynamic behaviour and also produced a simple model to predict their output [18]. Published research focuses mainly on the application of MEMS accelerometers for machine diagnostics, but a more in-depth understanding of sensing and signal processing for rotor-mounted accelerometers is still required to generate new methods for implementation and utilization.

The present study is based on a prototype system, which is described in Section 2. A theoretical framework for internal rotor-mounted sensing is then introduced, which determines the relation between accelerometer output signals and the motion of the rotor in the fixed frame. Calibration considerations are also examined. Simulated and experimental results, including steady state and transient dynamics, are evaluated. Finally, a technique is presented which allows the accelerometers to be used to measure rotational speed.

2. System description

The experimental rotor system designed for this study (Fig. 1) consists of a 90 cm long hollow steel shaft with a larger diameter central section, which houses the sensors. The outer diameter of the central section is 60 cm, whereas the thinner supporting shafts have an outer diameter of 20 cm. The first bending resonant frequency of the rotor, identified by impact testing, is 38.5 Hz (2,310 rpm). The rotor is horizontal, supported by rolling element bearings, and is flexibly coupled to a DC motor, which can achieve operating speeds of up to 3,000 rpm. Figure 2 shows a cross-section of the central shaft. The sensing module position, as well as the lock hubs that couple the larger and smaller sections, are indicated. Electrical power (3.7 V, 1 A) is provided through a mercury slipring, which can rotate at up to 3,200 rpm.

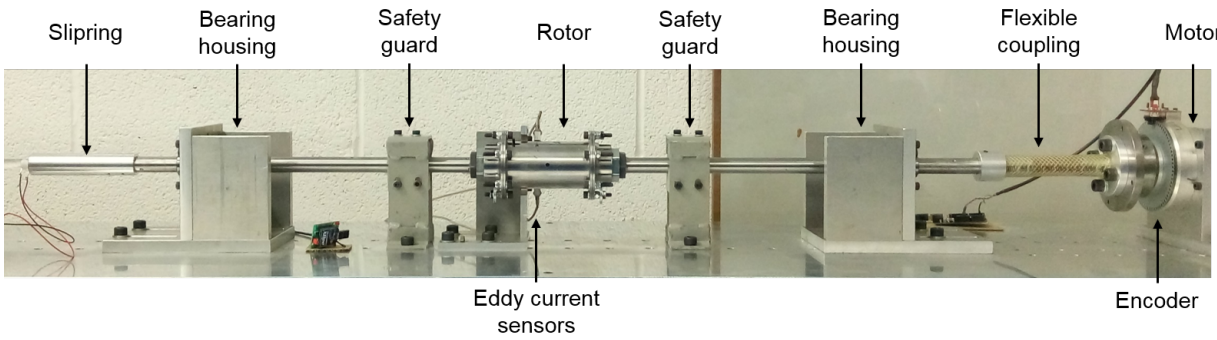

Figure 1: Test system for evaluating internal sensing strategies.

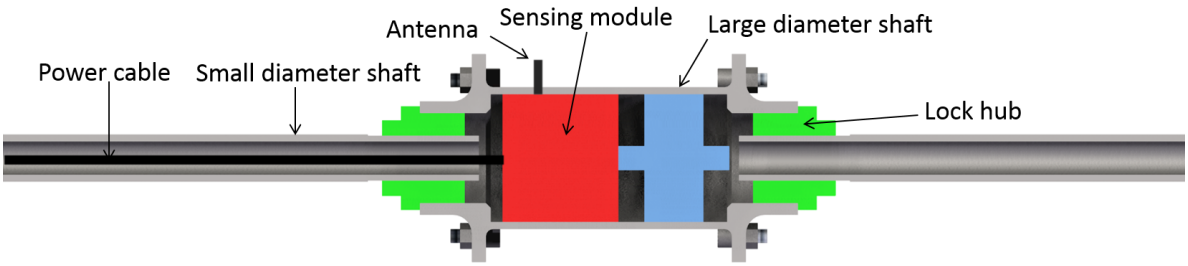

Figure 2: Cross-section of rotor.

2.1. Sensing module

The sensing module, shown in Fig. 3(a), contains two MEMS digital accelerometers (Analog Devices model ADXL362). These can measure acceleration in 3 perpendicular axes over a selectable range of ± (2, 4 or 8) g, with a resolution of ± (1, 2 or 4) mg, respectively (12-bit resolution). Their maximum sampling rate is 600 Hz and they can withstand accelerations up to 5,000 g. The required operating voltage is 3.3 V, with a current consumption in the μA range. Despite a small size (3 × 3 × 1 mm), the devices have a number of inbuilt features, including a 512 sample memory buffer, interrupt functions and internal temperature sensor. The accelerometers are mounted with their "Z" axes aligned with the longitudinal axis of the rotor. They are supported on a translating frame, which allows small changes to be made to their position within the rotor using small adjustment screws (Fig. 3(b)). The screws are accessible from the outside of the rotor, through the port holes labeled U and V in Fig. 4.

Aside from the accelerometers, the sensing module also contains a micro-controller with a clock speed of 8 MHz and a Zigbee-based wireless radio module, which enables transmission rates of up to 250 kbits/s. The antenna protrudes from the rotor as indicated in Fig. 2.

In practice, the geometry of a rotor with internal sensors is limited only by the size of the electronic components within. The evolution of the portable electronic device industry has led to

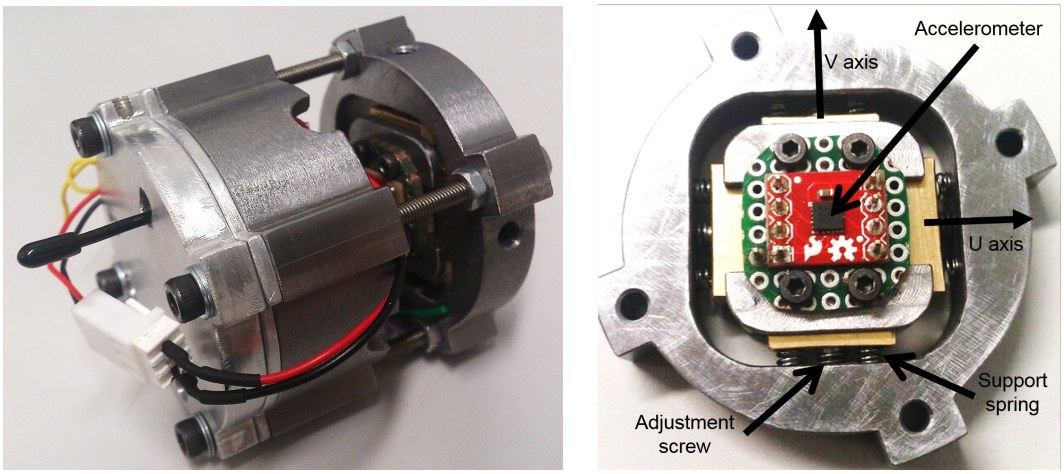

(a) Sensing module (b) Accelerometer and support frame

Figure 3: Internal rotor sensing module.

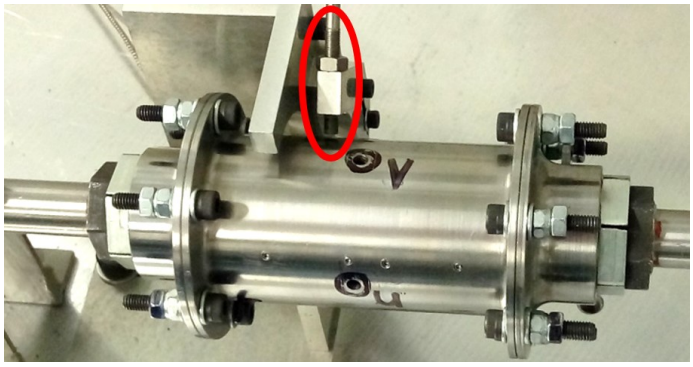

Figure 4: Eddy current displacement sensors. Accelerometer U and V axis adjustment port holes are indicated.

developments which allow extremely compact components and layouts to be achievable. In high speed applications, where high centrifugal loading might be expected, potting the electronics with a suitable compound would be an established technique to increase their durability under high stresses.

2.2. Stator-mounted sensors

A pair of stator-mounted eddy current displacement sensors (1 kHz sampling rate) were also installed in the prototype to provide a reference measurement of the rotor vibration. Figure 4 shows the position of the eddy current sensors as well as the U and V accelerometer axes. The measurement planes of both types of sensors are separated by 10 mm to prevent the accelerometer position adjustment port holes interfering with the eddy current sensors.

3. Theoretical framework

In this section, the framework for the analysis of rotating accelerometer signals is described. A brief overview of the principle of operation of the accelerometer is provided, followed by an analytical expression of the accelerometer signals in terms of the motion of the rotor. This is then used, together with a finite element model described in state space form, to study the orbit characteristics of whirling rotors, as measured by rotating accelerometers. The resulting analysis is then applied to the practical problem of extracting displacement-related information from the accelerometer signals.

3.1. Analysis of rotating accelerometer measurements

MEMS accelerometers consist of a proof mass suspended on spring mounts (represented schematically in Fig. 5(b)), and surrounded by capacitor plates. These are able to detect changes in capacitance when the proof mass moves under device acceleration. Whenever the resonance frequency of the support structure is much larger than the measured excitation frequency, quasi-static measurement conditions can be assumed, under which the motion of the proof mass will be dominated by the stiffness of the spring mounts. In this case, the acceleration of the accelerometer will be proportional to the displacement of its proof mass.

Figure 5(a) shows the cross-section of a rotor with geometric centre C and an internal accelerometer located at B. The position of the proof mass is denoted by P. Three distinct reference frames are defined:

(i) XY is the inertial reference frame corresponding to the stator. O_I is the equilibrium point for the rotor geometric centre at zero speed.

(ii) $U'V'$ is a rotating reference frame with origin at C that is rotated together with the rotor by an angle θ.

(iii) UV is a rotating reference frame centered on the accelerometer, which is translated relative to $U'V'$ by an offset displacement $\varepsilon_{u'v'}$.

In the notation used in this paper, if a parameter has components (α_u,α_v), its complex form is designated by $\alpha_{uv} = \alpha_u + \mathrm{j}\alpha_v$. Hence, $z_{uv} = (p_u - d_u) + \mathrm{j}(p_v - d_v)$ is the complex representation of the proof mass displacement relative to the accelerometer housing. Referring to Fig. 5(b) and resolving components into the inertial frame XY, the equation of motion of the proof mass is

$$m_p \ddot{z}_{xy} = -(k_a z_{uv} + c_a \dot{z}_{uv})\mathrm{e}^{\mathrm{j}\theta} - m_p(\ddot{d}_{xy} + \mathrm{j}g) \tag{1}$$

Equation (1) can be transformed to the accelerometer-fixed UV frame knowing that $z_{xy} = z_{uv}\mathrm{e}^{\mathrm{j}\theta}$. It follows that

$$\ddot{z}_{xy} = \left[\ddot{z}_{uv} + 2\mathrm{j}\dot{\theta}\dot{z}_{uv} + (\mathrm{j}\ddot{\theta} - \dot{\theta}^2)z_{uv}\right]\mathrm{e}^{\mathrm{j}\theta}$$

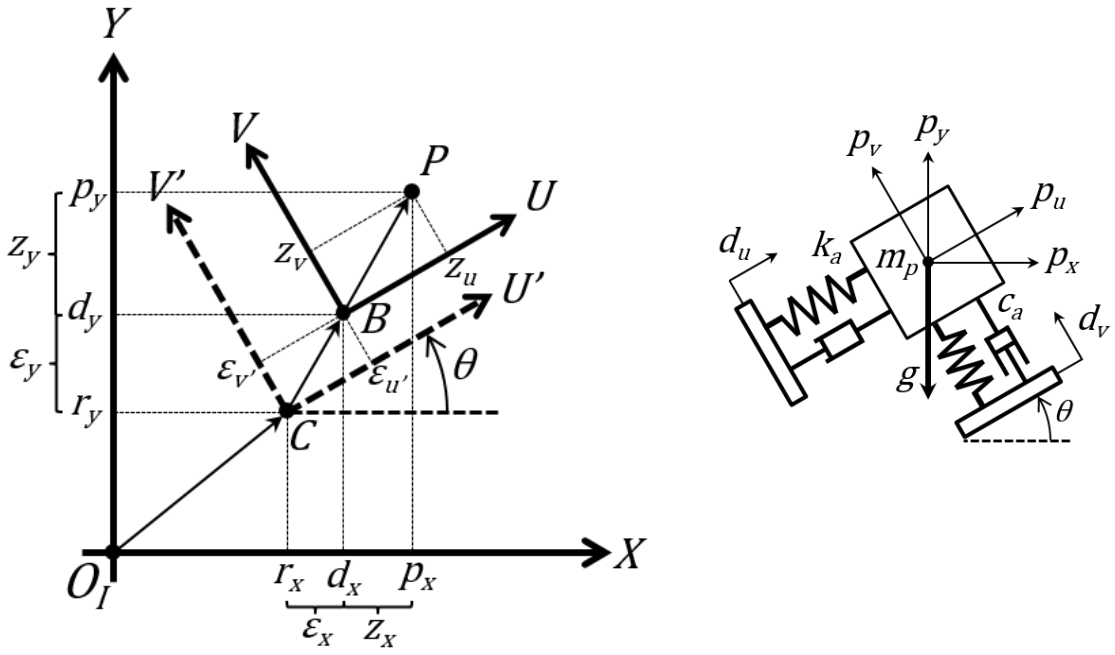

(a) Coordinate systems (b) Detail of accelerometer proof mass

Figure 5: Rotor cross-section diagram.

hence,

$$\left[\ddot{z}_{uv} + (2\mathrm{j}\dot{\theta} + \frac{\omega_r}{Q})\dot{z}_{uv} + (\mathrm{j}\ddot{\theta} - \dot{\theta}^2 + \omega_r^2)z_{uv}\right] \mathrm{e}^{\mathrm{j}\theta} = -(\ddot{d}_{xy} + \mathrm{j}g) \tag{2}$$

with $\omega_r = \sqrt{k_a/m_p}$ and $Q = \sqrt{k_a m_p}/c_a$. For steady speed $\ddot{\theta}$ is zero. The motion of the proof mass can be assumed to be quasi-static if the resonance frequency of the sprung structure ω_r is much larger than the excitation frequency $\dot{\theta}$. This can be demonstrated by considering a general harmonic motion of the proof mass in response to harmonic rotor motion, where z_{uv} takes the form of an infinite series of terms:

$$z_{uv} = \sum_{i=1}^{\infty} A_i \mathrm{e}^{\mathrm{j}f_i\dot{\theta}t} \tag{3}$$

where A_i is a complex amplitude and the product $f_i\dot{\theta}$ is the frequency of each harmonic component expressed in terms of the excitation frequency $\dot{\theta}$. Thus, the left hand term in Eq. (2) becomes

$$\sum_{i=1}^{\infty} \left[-(f_i^2 + 2f_i + 1)\frac{\dot{\theta}^2}{\omega_r^2} + \frac{\mathrm{j}f_i\dot{\theta}}{Q\omega_r} + 1\right] \omega_r^2 A_i \mathrm{e}^{\mathrm{j}f_i\dot{\theta}t}\mathrm{e}^{\mathrm{j}\theta} \tag{4}$$

If $\omega_r/\dot{\theta} \to \infty$, the bracketed term in Eq. (4) tends to 1, and hence the the proof mass motion will be dominated by the stiffness of the sprung structure, implying quasi-static motion. Thus, it can

be assumed that the first two terms in Eq. (2) are negligible and hence

$$\omega_r^2 z_{uv} \mathrm{e}^{\mathrm{j}\theta} \approx -(\ddot{d}_{xy} + \mathrm{j}g) \tag{5}$$

Under quasi-static conditions, the accelerometer output is defined as $a_m = -\omega_r^2 z_{uv}$ and so the relationship between the motion of the rotor-mounted accelerometer and its output signal is

$$a_m \approx (\ddot{d}_{xy} + \mathrm{j}g)\mathrm{e}^{-\mathrm{j}\theta} \tag{6}$$

In general, the accelerometer may be offset from C by a displacement $\varepsilon_{xy} = \varepsilon_{u'v'}\mathrm{e}^{\mathrm{j}\theta}$ where $\varepsilon_{u'v'}$ is a constant. In this case $d_{xy} = r_{xy} + \varepsilon_{xy}$. However, if $\varepsilon_{u'v'}$ is adjusted to be small (as detailed in Section 5.2), $U'V'$ coincides with UV and the displacement of the accelerometer is approximately that of the centre of the rotor, $d_{xy} \approx r_{xy}$, and hence a_m can be used to infer $\ddot{r}_{xy}$.

3.2. Orbit characteristics for rotating accelerometers

When rotating with constant speed such that $\theta = \omega t$, a rotor will describe an orbit around its equilibrium point (O_I in Fig. 5(a)). The whirl orbit will depend on the forcing inputs to the rotordynamic system and can be studied through the use of a finite element model, expressed in state space form. The matrix-vector equation of motion for the finite element model is

$$\mathbf{M}\ddot{\mathbf{q}} + [\mathbf{D_B} - \omega\mathbf{G}]\,\dot{\mathbf{q}} + \mathbf{K}\mathbf{q} = \mathbf{f} \tag{7}$$

where $\mathbf{q} = \{x_1,\, y_1,\, \varphi_{x1},\, \varphi_{y1},\, \ldots\,,\, x_n,\, y_n,\, \varphi_{xn},\, \varphi_{yn}\}^{\mathrm{T}}$ is a vector containing the displacement and rotations states of the n nodes of the finite element model , $\mathbf{M}$ is the mass matrix containing terms for translational and rotational inertia, $\mathbf{D_B}$ is the damping matrix representing the bearings, ω is the angular speed of the rotor, $\mathbf{G}$ is the skew-symmetric gyroscopic matrix, $\mathbf{K}$ is the stiffness matrix, and $\mathbf{f}$ is a vector containing the external forces and moments applied to the rotor. Other rotordynamic effects such as spin-softening and stress-stiffening are negligible in the range of operating speeds considered for the prototype rotor in Fig. 1.

The equation of motion can be expressed in the state space form through $\mathbf{z}_1 = \mathbf{q}$ and $\mathbf{z}_2 = \dot{\mathbf{z}}_1$. For a state vector $\mathbf{z} = [\mathbf{z}_1^{\mathrm{T}}, \mathbf{z}_2^{\mathrm{T}}]^{\mathrm{T}}$,

$$\begin{aligned} \dot{\mathbf{z}} &= \mathbf{A}\mathbf{z} + \mathbf{B}\mathbf{u} \\ \mathbf{y} &= \mathbf{C}\mathbf{z} + \mathbf{D}\mathbf{u} \end{aligned} \tag{8}$$

with $\mathbf{u} = \mathbf{f}$ and

$$\mathbf{A} = \begin{bmatrix} \mathbf{0} & \mathbf{I} \\ -\mathbf{M}^{-1}\mathbf{K} & -\mathbf{M}^{-1}\left[\mathbf{D_B} - \omega\mathbf{G}\right] \end{bmatrix} \quad , \quad \mathbf{B} = \begin{bmatrix} \mathbf{0} \\ \mathbf{M}^{-1} \end{bmatrix}$$

Considering the nodal accelerations as outputs, $\mathbf{y} = \dot{\mathbf{z}}_2$, hence

$$\mathbf{C} = \begin{bmatrix} -\mathbf{M}^{-1}\mathbf{K} & -\mathbf{M}^{-1}\left[\mathbf{D_B} - \omega\mathbf{G}\right] \end{bmatrix} \quad , \quad \mathbf{D} = \mathbf{M}^{-1}$$

The rotor response can be derived from the state space model in Eq. (8), which has a general solution

$$\mathbf{z}(t) = \mathrm{e}^{\mathbf{A}t}\mathbf{z}(0) + \int_0^t \mathrm{e}^{\mathbf{A}(t-\tau)}\mathbf{B}\mathbf{u}(\tau)\,\mathrm{d}\tau \tag{9}$$

If the eigenvalue/vector problem is solved to yield $\mathbf{AV} = \mathbf{V}\boldsymbol{\Lambda}$ with

$$\mathbf{V} = \begin{bmatrix} \mathbf{v}_1 & \mathbf{v}_{-1} & \dots & \mathbf{v}_{4n} & \mathbf{v}_{-4n} \end{bmatrix}_{(8n\times 8n)} \quad , \quad \boldsymbol{\Lambda} = \mathrm{diag}\left(\lambda_1, \lambda_{-1}, \dots, \lambda_{4n}, \lambda_{-4n}\right) \quad , \quad \lambda_{-m} = \lambda_m^*$$

and the state vector is transformed according to $\mathbf{z} = \mathbf{V}\mathbf{p}$, then the state space equation becomes

$$\dot{\mathbf{p}} = \boldsymbol{\Lambda}\mathbf{p} + \hat{\mathbf{B}}\mathbf{u} \tag{10}$$

where $\hat{\mathbf{B}} = \mathbf{V}^{-1}\mathbf{B}$. Then

$$\mathbf{p}(t) = \mathrm{e}^{\boldsymbol{\Lambda}t}\mathbf{p}(0) + \int_0^t \mathrm{e}^{\boldsymbol{\Lambda}(t-\tau)}\hat{\mathbf{B}}\mathbf{u}(\tau)\,\mathrm{d}\tau \tag{11}$$

Since

$$\mathrm{e}^{\boldsymbol{\Lambda}t} = \mathrm{diag}(\mathrm{e}^{\lambda_1 t}, \mathrm{e}^{\lambda_{-1} t}, \dots, \mathrm{e}^{\lambda_{4n} t}, \mathrm{e}^{\lambda_{-4n} t}) \tag{12}$$

it follows that the modal states are given by

$$p_m(t) = \mathrm{e}^{\lambda_m t}p_m(0) + \hat{\mathbf{b}}_m^{\mathrm{T}} \int_0^t \mathrm{e}^{\lambda_m(t-\tau)}\mathbf{u}(\tau)\,\mathrm{d}\tau \tag{13}$$

where $\hat{\mathbf{b}}_m$ contains the transposed m^{th} row of $\hat{\mathbf{B}}$. The r^{th} state can therefore be expressed as

$$z_r(t) = \sum_{m=-4n}^{4n} v_{rm}\mathrm{e}^{\lambda_m t}p_m(0) + \sum_{m=-4n}^{4n} v_{rm}\hat{\mathbf{b}}_m^{\mathrm{T}} \int_0^t \mathrm{e}^{\lambda_m(t-\tau)}\mathbf{u}(\tau)\,\mathrm{d}\tau \tag{14}$$

If every eigenvalue has a negative real part (stable rotor system), the first summation of modal terms arising from initial conditions will decay to zero. The second summation involves a convolution integral of modal terms with each input component. The position of the rotor centre at the point of interest for the accelerometer plane is given in terms of Eq. (14) as $d_{xy}(t) = z_r(t) + \mathrm{j}z_s(t)$ for an appropriate choice of r and $s = r + 1$. Hence, the displacement and acceleration of the accelerometer in the inertial reference frame will be, respectively,

$$d_{xy}(t) = \sum_{m=-4n}^{4n} \left(v_{rm} + \mathrm{j}v_{sm}\right) p_m(0)\mathrm{e}^{\lambda_m t} + \sum_{m=-4n}^{4n} (v_{rm} + \mathrm{j}v_{sm})\hat{\mathbf{b}}_m^{\mathrm{T}} \int_0^t \mathrm{e}^{\lambda_m(t-\tau)}\mathbf{u}(\tau)\,\mathrm{d}\tau \tag{15}$$

$$\ddot{d}_{xy}(t) = \sum_{m=-4n}^{4n} \lambda_m^2 \left(v_{rm} + \mathrm{j}v_{sm}\right) p_m(0) \mathrm{e}^{\lambda_m t} + \sum_{m=-4n}^{4n} \left(v_{rm} + \mathrm{j}v_{sm}\right) \hat{\mathbf{b}}_m^{\mathrm{T}} \left(\lambda_m^2 \int_0^t \mathrm{e}^{\lambda_m (t-\tau)} \mathbf{u}(\tau)\, \mathrm{d}\tau + \lambda_m \mathbf{u}(t) + \dot{\mathbf{u}}(t) \right) \tag{16}$$

Combining Eqs. (6) and (16) gives the corresponding accelerometer signal

$$a_m(t) = \sum_{m=-4n}^{4n} \lambda_m^2 \left(v_{rm} + \mathrm{j}v_{sm}\right) p_m(0) \mathrm{e}^{(\lambda_m - \mathrm{j}\omega)t} + \sum_{m=-4n}^{4n} \left(v_{rm} + \mathrm{j}v_{sm}\right) \hat{\mathbf{b}}_m^{\mathrm{T}} \left(\lambda_m^2 \int_0^t \mathrm{e}^{\lambda_m (t-\tau)} \mathbf{u}(\tau)\, \mathrm{d}\tau + \lambda_m \mathbf{u}(t) + \dot{\mathbf{u}}(t) \right) \mathrm{e}^{-\mathrm{j}\omega t} + \mathrm{j}g\mathrm{e}^{-\mathrm{j}\omega t} \tag{17}$$

A single frequency harmonic input has the form

$$\mathbf{u}(t) = \boldsymbol{\mu} \mathrm{e}^{\mathrm{j}\gamma t} + \boldsymbol{\mu}^* \mathrm{e}^{-\mathrm{j}\gamma t} \tag{18}$$

Knowing that

$$\int_0^t \mathrm{e}^{\lambda_m (t-\tau)} \mathbf{u}(\tau)\, \mathrm{d}\tau = \frac{\boldsymbol{\mu}}{(-\lambda_m + \mathrm{j}\gamma)} \left(\mathrm{e}^{\mathrm{j}\gamma t} - \mathrm{e}^{\lambda_m t} \right) + \frac{\boldsymbol{\mu}^*}{(-\lambda_m - \mathrm{j}\gamma)} \left(\mathrm{e}^{-\mathrm{j}\gamma t} - \mathrm{e}^{\lambda_m t} \right) \tag{19}$$

the rotor orbit in response to periodic force inputs, once all transient terms have decayed away, is given by

$$d_{xy}(t) = \sum_{m=-4n}^{4n} \left(v_{rm} + \mathrm{j}v_{sm}\right) \hat{\mathbf{b}}_m^{\mathrm{T}} \left(\frac{\boldsymbol{\mu}}{(-\lambda_m + \mathrm{j}\gamma)} \mathrm{e}^{\mathrm{j}\gamma t} + \frac{\boldsymbol{\mu}^*}{(-\lambda_m - \mathrm{j}\gamma)} \mathrm{e}^{-\mathrm{j}\gamma t} \right) \tag{20}$$

This expression can be written in the compact form

$$d_{xy}(t) = R_F \mathrm{e}^{\mathrm{j}(\gamma t + \phi_F)} + R_B \mathrm{e}^{\mathrm{j}(-\gamma t + \phi_B)} \tag{21}$$

where the rotor orbit is described in terms of forward and backward whirls of radii R_F and R_B and phases ϕ_F and ϕ_B, respectively, given by

$$R_F(\gamma, \boldsymbol{\mu}) = \left| \sum_{m=-4n}^{4n} \left(v_{rm} + \mathrm{j}v_{sm}\right) \hat{\mathbf{b}}_m^{\mathrm{T}} \frac{\boldsymbol{\mu}}{(-\lambda_m + \mathrm{j}\gamma)} \right|, \; \phi_F(\gamma, \boldsymbol{\mu}) = \arg \left(\sum_{m=-4n}^{4n} \left(v_{rm} + \mathrm{j}v_{sm}\right) \hat{\mathbf{b}}_m^{\mathrm{T}} \frac{\boldsymbol{\mu}}{(-\lambda_m + \mathrm{j}\gamma)} \right)$$

$$R_B(\gamma, \boldsymbol{\mu}^*) = \left| \sum_{m=-4n}^{4n} \left(v_{rm} + \mathrm{j}v_{sm}\right) \hat{\mathbf{b}}_m^{\mathrm{T}} \frac{\boldsymbol{\mu}^*}{(-\lambda_m - \mathrm{j}\gamma)} \right|, \; \phi_B(\gamma, \boldsymbol{\mu}^*) = \arg \left(\sum_{m=-4n}^{4n} \left(v_{rm} + \mathrm{j}v_{sm}\right) \hat{\mathbf{b}}_m^{\mathrm{T}} \frac{\boldsymbol{\mu}^*}{(-\lambda_m - \mathrm{j}\gamma)} \right)$$

The associated accelerometer signal will be

$$a_m = -\gamma^2 R_F \mathrm{e}^{\mathrm{j}((\gamma - \omega)t + \phi_F)} - \gamma^2 R_B \mathrm{e}^{\mathrm{j}(-(\gamma + \omega)t + \phi_B)} + \mathrm{j}g\mathrm{e}^{-\mathrm{j}\omega t} \tag{22}$$

For a general input consisting of unbalance and other sources of vibration,

$$\mathbf{u}(t) = \omega^2 \boldsymbol{\sigma} \mathrm{e}^{\mathrm{j}\omega t} + \omega^2 \boldsymbol{\sigma}^* \mathrm{e}^{-\mathrm{j}\omega t} + \mathbf{u}_{res}(t) \tag{23}$$

where $\boldsymbol{\sigma}$ is a complex mass-eccentricity unbalance vector and $\mathbf{u}_{res}$ indicates the residual forcing produced by the remaining input sources. Thus, the displacement in the inertial reference frame and the corresponding accelerometer output for a general rotor will be

$$d_{xy} = R_{F\sigma} \mathrm{e}^{\mathrm{j}(\omega t + \phi_{F\sigma})} + R_{B\sigma} \mathrm{e}^{\mathrm{j}(-\omega t + \phi_{B\sigma})} + \sum_{m=-4n}^{4n} (v_{rm} + \mathrm{j} v_{sm}) \hat{\mathbf{b}}_m^{\mathrm{T}} \int_0^t \mathrm{e}^{\lambda_m (t-\tau)} \mathbf{u}_{res}(\tau) \, \mathrm{d}\tau \tag{24}$$

$$\begin{aligned} a_m = & -\omega^2 R_{F\sigma} \mathrm{e}^{\mathrm{j}\phi_{F\sigma}} - \omega^2 R_{B\sigma} \mathrm{e}^{\mathrm{j}(-2\omega t + \phi_{B\sigma})} + \mathrm{j} g \mathrm{e}^{-\mathrm{j}\omega t} \\ & + \sum_{m=-4n}^{4n} (v_{rm} + \mathrm{j} v_{sm}) \hat{\mathbf{b}}_m^{\mathrm{T}} \left(\lambda_m^2 \int_0^t \mathrm{e}^{\lambda_m (t-\tau)} \mathbf{u}_{res}(\tau) \, \mathrm{d}\tau + \lambda_m \mathbf{u}_{res}(t) + \dot{\mathbf{u}}_{res}(t) \right) \mathrm{e}^{-\mathrm{j}\omega t} \end{aligned} \tag{25}$$

with $R_{F\sigma} = R_F(\omega, \omega^2 \boldsymbol{\sigma})$, $R_{B\sigma} = R_B(\omega, \omega^2 \boldsymbol{\sigma}^*)$, $\phi_{F\sigma} = \phi_F(\omega, \omega^2 \boldsymbol{\sigma})$ and $\phi_{B\sigma} = \phi_B(\omega, \omega^2 \boldsymbol{\sigma}^*)$. In the inertial frame displacement orbit, the first term can be understood to form a base circular orbit of radius $R_{F\sigma}$, with all other signal components being deviations therefrom. In this way, the presence of the second term would produce an elliptical orbit. Any remaining periodic terms are related to non-synchronous vibration sources, such as bearing race faults or rotor-stator contact. In the "acceleration orbit" measured by the rotating accelerometers the first term expresses the centripetal acceleration experienced by the rotor centre, which has zero frequency. The second term and the term associated with the gravitational acceleration both produce counter-rotating vectors, with frequencies -2ω and $-\omega$, respectively.

3.2.1. Example orbits

For a rotordynamic system excited only by unbalance the accelerometer displacement in the inertial reference frame and the signal produced by the accelerometer are

$$d_{xy} = R_{F\sigma} \mathrm{e}^{\mathrm{j}(\omega t + \phi_{F\sigma})} + R_{B\sigma} \mathrm{e}^{\mathrm{j}(-\omega t + \phi_{B\sigma})} \tag{26}$$

$$a_m = -\omega^2 R_{F\sigma} \mathrm{e}^{\mathrm{j}\phi_{F\sigma}} - \omega^2 R_{B\sigma} \mathrm{e}^{\mathrm{j}(-2\omega t + \phi_{B\sigma})} + \mathrm{j} g \mathrm{e}^{-\mathrm{j}\omega t} \tag{27}$$

Equation (26) describes an elliptical orbit, in which the semi-major and semi-minor axes are $R_{F\sigma} + R_{B\sigma}$ and $R_{F\sigma} - R_{B\sigma}$, respectively. In the special case where $R_{F\sigma} \gg R_{B\sigma}$, the rotor approximates the idealised circular orbit.

Example plots for two different orbits are presented in Figs. 6 and 7. The orbits are shown as a "displacement orbit" viewed from the inertial reference frame (as typically obtained from eddy

current displacement sensors) and as an "acceleration orbit", observed by internally mounted accelerometers (i.e. $\mathrm{Im}(a_m)$ vs. $\mathrm{Re}(a_m)$). Figures 6(a) and 6(b) show an unbalance-induced elliptical orbit whereas Figs. 7(a) and 7(b) show a multi-frequency case, which includes two additional super-synchronous periodic forcing inputs. In both cases the "acceleration orbits" are not centered at the origin due to the presence of the synchronous component $-\omega^2 R_{F\sigma} \mathrm{e}^{\mathrm{j}\phi_{F\sigma}}$. This component is highlighted in the accelerometer orbit figures, appearing as a single point. The parameters which define each orbit can be found in Table 1.

3.3. Extracting orbit radius from acceleration measurements

This subsection considers how to extract information about the size of the displacement orbits directly from accelerometer signals. Integration of the acceleration signal to obtain displacement is possible, but is sensitive to initial conditions and offset errors [19]. Because of this, an integration-free method is presented.

A low-pass filter may be applied to the acceleration signal to reduce the gravitational acceleration and other high-frequency terms appearing in Eq. (25). This filtered acceleration signal will approximate the mean value,

$$\bar{a}_m = -\omega^2 R_{F\sigma} \mathrm{e}^{\mathrm{j}\phi_{F\sigma}} \tag{28}$$

A corresponding mean complex radius parameter may be calculated from $\bar{a}_m$ and ω as

$$d_m = d_{mu} + \mathrm{j} d_{mv} = -\frac{\bar{a}_m}{\omega^2} = R_{F\sigma} \mathrm{e}^{\mathrm{j}\phi_{F\sigma}} \tag{29}$$

The magnitude of this parameter, $|d_m|$, yields the displacement amplitude of the idealised base circular orbit, $R_{F\sigma}$. For the simple case of a circular orbit $|d_{xy}| = R_{F\sigma}$, and therefore the radius of orbit of the rotor can be directly inferred from the accelerometer measurements with the use of a simple low-pass filter. For non-circular orbits, the instantaneous orbit radius $|d_{xy}|$ is not constant, but the parameter $|d_m|$ provides a good estimate of its mean value for rotors whose behaviour is dominated by unbalance. The mean value of the instantaneous radius is given by

$$\overline{|d_{xy}|} = \frac{\omega}{2\pi} \int_0^{\frac{2\pi}{\omega}} |d_{xy}| \, \mathrm{d}t \tag{30}$$

For an elliptical orbit, d_{xy} is given by Eq. (26) and so

$$\overline{|d_{xy}|} = \frac{\omega}{2\pi} \int_0^{\frac{2\pi}{\omega}} \sqrt{R_{F\sigma}^2 + R_{B\sigma}^2 + 2R_{F\sigma}R_{B\sigma}\cos(2\omega t + \phi_{F\sigma} - \phi_{B\sigma})} \, \mathrm{d}t \tag{31}$$

This can be expressed as

$$\overline{|d_{xy}|} = \frac{R_{F\sigma}(1+\eta)}{2\pi} \left[E(\beta|m) - E(\alpha|m) \right] \tag{32}$$

Table 1: Parameters of orbits shown in Figs. 6 and 7.

	Orbit parameters					
	ω (rad s^{-1})	γ_σ (rad s^{-1})	$R_{F\sigma}$ (mm)	$R_{B\sigma}$ (mm)	$\phi_{F\sigma}$ (°)	$\phi_{B\sigma}$ (°)
Elliptical	209.4	ω	0.48	0.1	234	-261
Multi-frequency	52.4	$\omega/2\omega/7\omega$	0.48/0.12/0.03	0.1/0.05/0.02	234/20/-47	-261/15/-136

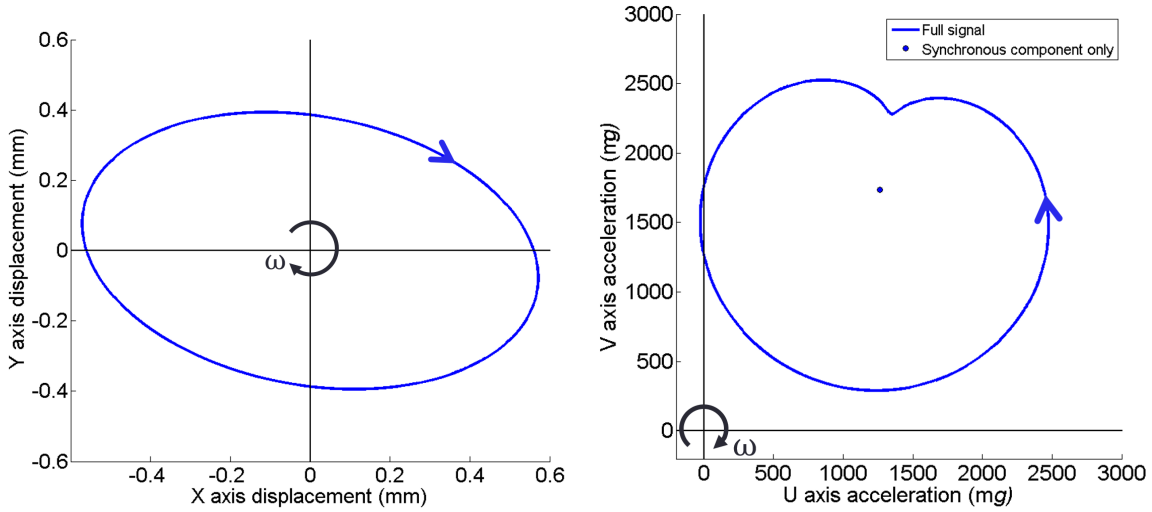

(a) Inertial reference frame (b) Accelerometer output

Figure 6: Theoretical single-frequency elliptical rotor orbit, as would be measured with stator-mounted displacement sensors and rotor-mounted accelerometers.

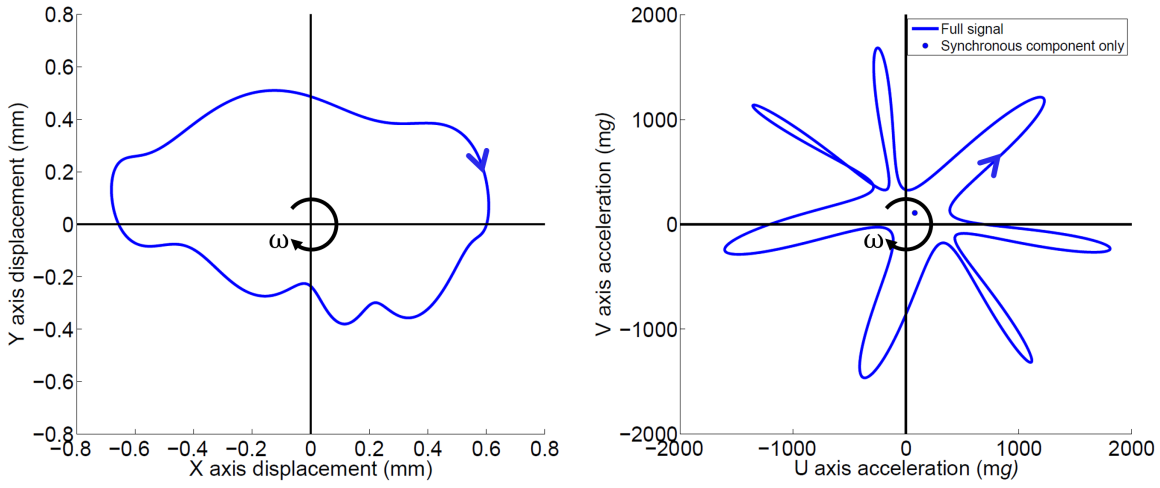

(a) Inertial reference frame (b) Accelerometer output

Figure 7: Theoretical multi-frequency arbitrary rotor orbit, as would be measured with stator-mounted displacement sensors and rotor-mounted accelerometers

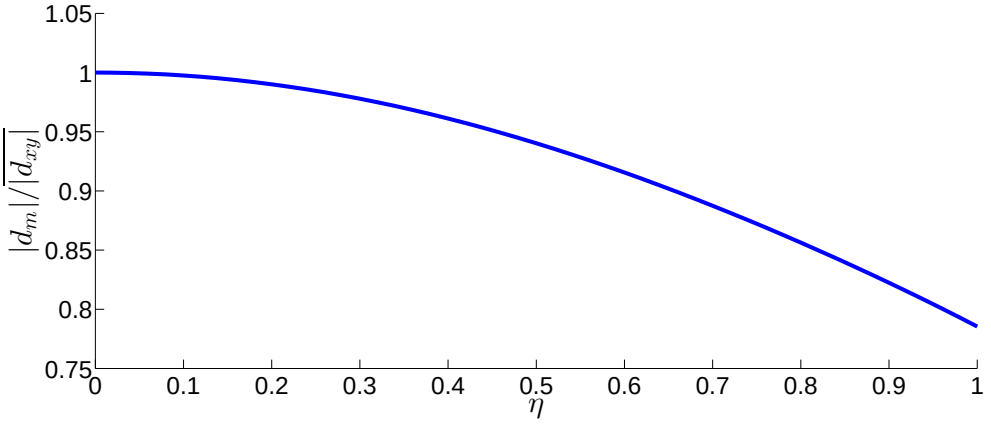

Figure 8: Variation of $|d_m|/\overline{|d_{xy}|}$ as a function of the deviation ratio $\eta = R_{B\sigma}/R_{F\sigma}$ for an elliptical orbit.

where

$$\eta = \frac{R_{B\sigma}}{R_{F\sigma}} \quad , \quad \beta = 2\pi + \frac{\phi_{F\sigma} - \phi_{B\sigma}}{2} \quad , \quad \alpha = \frac{\phi_{F\sigma} - \phi_{B\sigma}}{2} \quad , \quad m = \frac{4\eta}{(1+\eta)^2}$$

and $E(\alpha|m)$ is the incomplete elliptic integral of the second kind in the form

$$E(a|m) = \int_0^a \sqrt{1 - m\sin^2(\xi)}\,\mathrm{d}\xi$$

Figure 8 presents the ratio $|d_m|/\overline{|d_{xy}|}$ as a function of deviation ratio η for an elliptical orbit. For small η, that is, small deviation from the ideal circular orbit, $\overline{|d_{xy}|} \approx |d_m|$. Hence, the parameter $|d_m|$, obtained by applying a simple low-pass filter to an accelerometer signal and dividing by $-\omega^2$, will provide a good estimate of the average radius of orbit of rotors whose behaviour is dominated by unbalance, without the need for complex and time-consuming transformations. As an example, the $|d_m|/\overline{|d_{xy}|}$ ratio for the orbits presented in Figs. 6 and 7 are 0.989 and 0.974, respectively.

4. Model predictions

A finite element model of the experimental system has been produced to allow a numerical study of predicted behaviour. The rotor material is steel and the sensing module was considered as an additional mass of 2 kg. A schematic of the model is shown in Fig. 9. The bearing model parameters are given in Table 2. A 10-element model predicts first and second flexural modes at 38.5 Hz and 103.2 Hz, respectively. The corresponding zero-speed mode shapes are presented in Fig. 10.

In order to produce the desired rotating accelerometer output, Eq. (6) was used to convert the inertial frame acceleration vector expressed by $\mathbf{y}$ into the accelerometer signal vector so that

$$\mathbf{a}_m = \mathbf{E}[\mathbf{y} + \mathbf{W}g] \tag{33}$$

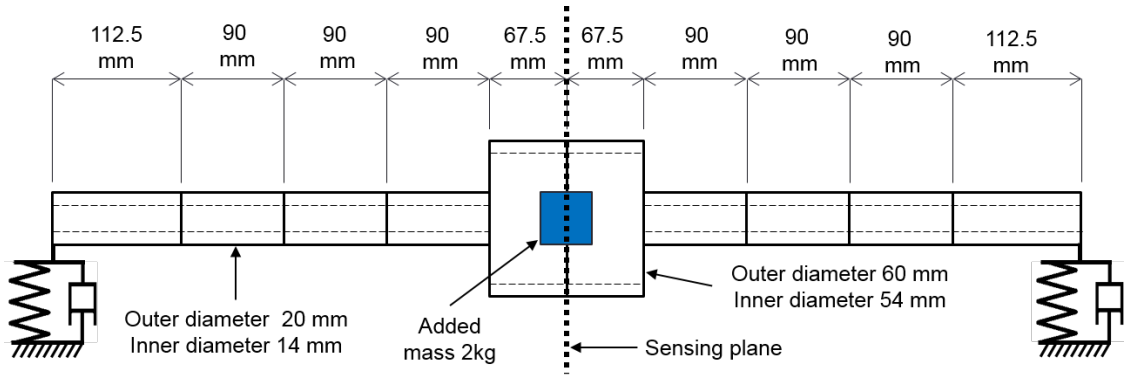

Figure 9: Finite element model of the prototype rotor.

Table 2: Finite element model parameters for bearing assembly.

Parameter	**Value**	**Unit**
Net stiffness - X	3×10^5	N m^{-1}
Net stiffness - Y	4×10^5	N m^{-1}
Net stiffness - Φ_Y	2.8×10^3	N m rad^{-1}
Net stiffness - Φ_X	2.8×10^3	N m rad^{-1}
Net damping - X	1×10^2	N s m^{-1}
Net damping - Y	1×10^2	N s m^{-1}

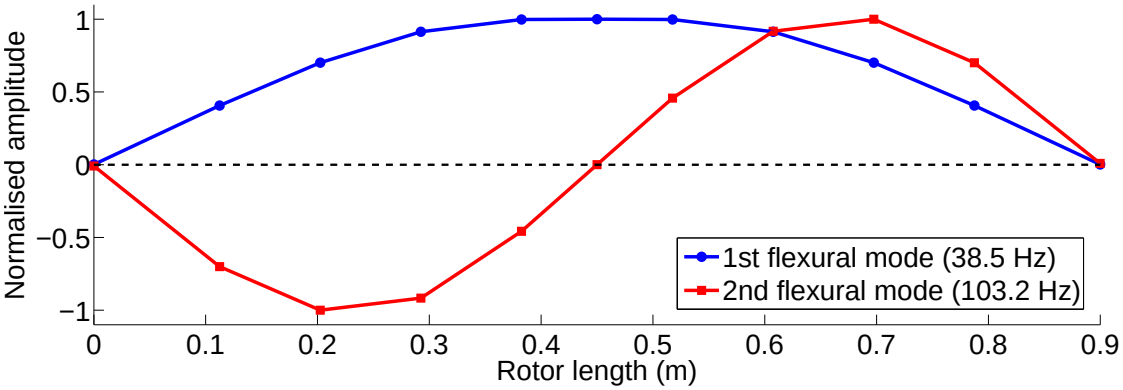

Figure 10: First and second flexural modes at zero speed, predicted by the finite element model.

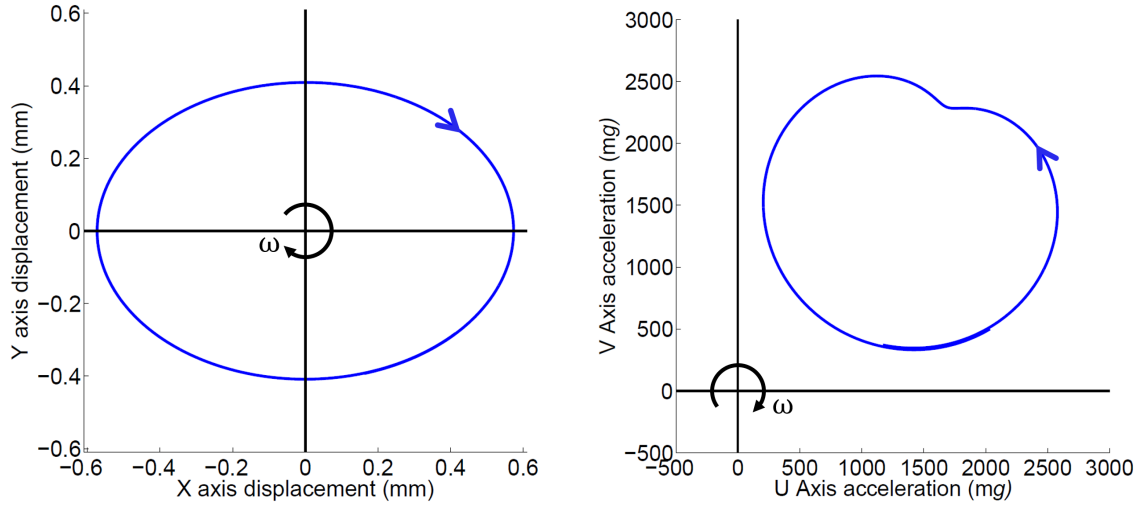

(a) Inertial reference frame

(b) Accelerometer output

Figure 11: Simulated rotor orbit at 2,000 rpm, as would be measured with stator-mounted displacement sensors and rotor-mounted accelerometers.

where $\mathbf{W} = [0 \quad 1 \quad 0 \quad 0 \quad \ldots \quad 0 \quad 1 \quad 0 \quad 0]^{\mathrm{T}}_{4n\times 1}$ and $\mathbf{E}$ is a $2n \times 4n$ block diagonal matrix with n basis blocks of the form

$$\mathbf{T} = \begin{bmatrix} \cos\omega t & \sin\omega t & 0 & 0 \\ -\sin\omega t & \cos\omega t & 0 & 0 \end{bmatrix}$$

The model was used to simulate the rotor operating at 2,000 rpm on supports with asymmetric stiffness and an unbalance of 250 g mm in the U and V planes, at the mid-point of the rotor length. The predicted rotor orbit viewed from the inertial reference frame is given in Fig. 11(a), while Fig. 11(b) shows the modelled accelerometer signals.

5. Calibration

The internal accelerometer measurements may be subject to two main sources of error, which must be compensated during operation: zero-g output offset and positional offset. The former is observed as the non-zero output when the accelerometer is subjected to zero-g (free-fall), and is a consequence of variability during manufacture. The latter is related to the positional difference ε_{xy} between the accelerometer and the geometric centre of the rotor (Fig. 5(a)). Techniques for reducing these offsets are now described.

5.1. Zero-g offsets

For a rotating accelerometer the zero-g offset can be significant, particularly at low speeds for which centripetal acceleration is small. To reduce the associated error, a complex correction term

$k = k_u + \mathrm{j}k_v$ is introduced:

$$d_c = d_m + \frac{k}{\omega^2} \tag{34}$$

The value of k is calculated based on the principle that, at low speeds, the effect of unbalance on the rotor response is negligible, and so there should be little variation in the U and V plane components of the rotor orbit over a set of different speeds. Thus, the real and imaginary parts of d_m can be evaluated at different and suitably low speeds, and a least squares formulation used to obtain values of k_u and k_v that minimise S_u and S_v, respectively, with

$$\begin{aligned} Su &= \sum_{i=1}^{l-1} \sum_{j=i+1}^{l} \left[\mathrm{Re}(d_{ci} - d_{cj})\right]^2 \\ Sv &= \sum_{i=1}^{l-1} \sum_{j=i+1}^{l} \left[\mathrm{Im}(d_{ci} - d_{cj})\right]^2 \end{aligned} \tag{35}$$

where the values corresponding to each of the l speeds are denoted by subscripts $i = 1, 2, \ldots, l-1$ and $j = i+1, i+2, \ldots, l$. The value of k is calculated as

$$k = \frac{P}{Q} \tag{36}$$

where

$$P = \sum_{i=1}^{l-1} \sum_{j=i+1}^{l} (d_{mi} - d_{mj}) \left(\frac{1}{\omega_i^2} - \frac{1}{\omega_j^2} \right) \tag{37}$$

$$Q = \sum_{i=1}^{l-1} \sum_{j=i+1}^{l} \left(\frac{1}{\omega_i^2} - \frac{1}{\omega_j^2} \right)^2 \tag{38}$$

To assess the procedure, experimental results were taken from the prototype rotor, with $l = 3$ and d_m measurements taken at 200, 300 and 400 rpm. Figure 12 shows the radius of orbit of the rotor over the operating speed range, as measured with the eddy current displacement sensors and estimated with the internal accelerometers, both with and without corrections ($|d_c|$ and $|d_m|$, respectively). The data for both types of sensor correlate very closely at high speeds in all cases. At low speeds, however, the uncorrected accelerometer-based data produce an obviously incorrect trend. The improvement achieved with the correction in Eq. (34) is clear, since the results align with the eddy current measurements.

5.2. Positional offset

Although the positional offset ε_{xy}, if known, can be compensated for numerically when analysing the accelerometer data, it is desirable to minimise it's magnitude to help prevent sensor saturation caused by excessive centripetal acceleration. To achieve this, the central shaft section containing

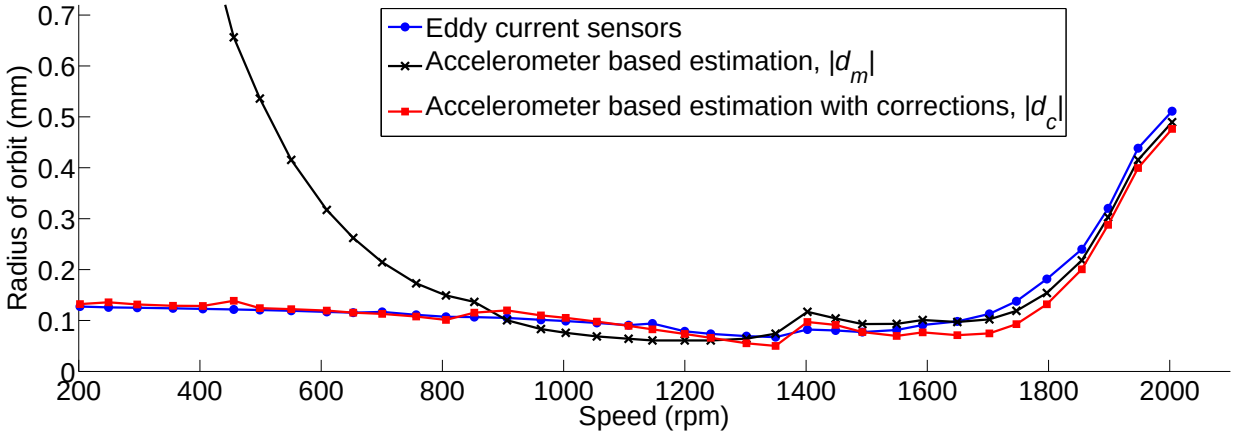

Figure 12: Orbit radius estimations derived from internal accelerometer measurements subject to zero -g offsets. Comparison between corrected and uncorrected data, and eddy current sensor measurements.

the sensing module was spun on a lathe over a range of speeds and the acceleration measured. If the lathe is assumed to be free of vibration, the mean value of the acceleration measured by the accelerometer will be related only to positional offset. The corresponding displacement parameter, d_c, for the measured orbit was calculated from the accelerometer signal and the position of the support frame in Fig. 3(b) was then adjusted by $-d_c$ to minimise $|\varepsilon_{xy}|$. This calibration process was repeated until the positional offset magnitude was suitably small (< 10 μm).

6. Experimental results

Experimental results are presented involving two important scenarios: steady-state vibration with periodic orbits, and transient vibration induced by impact under steady rotation. Further test results are presented that show how gravitational acceleration can be used to infer rotational speed for horizontal rotors.

For sufficiently low rotational speeds, acceleration measurements will be dominated by the synchronous counter-rotating component caused by gravity. At higher speeds, however, actual vibration information is more clearly evident. Figure 13(a) presents the X and Y axis eddy current displacement sensor data for steady rotation at 2,000 rpm, which shows a near elliptical orbit. The counterpart data provided by the accelerometers (Fig. 13(b)) shows a limaçon, not centred at the axis origin. The characteristics of these measured rotor orbits correlate with the theoretical and simulated orbits shown in Figs. 6 and 11.

6.1. Steady state: unbalance response measurement

Accelerometer and eddy current displacement sensor data were collected under steady state operation at speeds between 200 and 2,000 rpm (recorded in steps of 50 rpm). The test was

Table 3: Zero-g offset corrections for each axis of each accelerometer.

Axis	U1	U2	V1	V2
Value (mg)	-174.4	-167.6	-70.0	-102.3

repeated for three different unbalance conditions, illustrated in Fig. 14.

The accelerometer signals were converted into a corrected displacement signal, d_c, by applying a low-pass filter to the raw data, scaling by $-\omega^2$ and correcting for offset error (Eqs. (29) and (34)). The low-pass filter serves to eliminate the synchronous gravitational acceleration as well as other non-synchronous vibration. The required zero-g offset corrections were calculated following the procedure described in Section 5.1 and are given in Table 3, for each axis (U,V) of each of the two accelerometers (1,2).

Figure 15 compares the displacement parameter $|d_c|$ with the mean orbit radius measured by eddy current probes. The accelerometer and eddy current sensor data correlate well, showing an increase in rotor orbit size as the speed approaches the resonant frequency (2,310 rpm). The low speed radius of orbit is around 125 μm as the rotor assembly is not perfectly straight. These results confirm that, for a small positional offset ε_{xy}, the displacement signal d_c gives the mean steady state position of the geometric centre of the rotor in the rotating frame of reference.

6.1.1. Phase response measurement

The displacement parameter, d_c, indicates how the position of the rotor centre evolves with changes in operating condition, and comprises U and V axis displacement magnitude and phase information. As an example, Unbalance conditions 1 and 3 produce similar orbit magnitudes, as shown in Fig. 15, but the associated rotor responses have different phases. This is clearly observable in Fig. 16, which compares the U and V components of d_c for the three unbalance cases, showing data from 1,000 to 2,000 rpm. The advantage highlighted here is that phase information has been derived directly, without the need for key phasor sensing.

As the rotor speed approaches the critical speed, increasing phase lag is observed. In the rotating frame of reference the loci follow the typical resonance curve seen in a polar plot of synchronous vibration. This is illustrated by comparing the recorded data against the behaviour predicted by the finite element model, shown in Fig. 17(a). A detailed comparison of data for speeds up to 2,000 rpm is presented in Fig. 17(b).

6.2. Transient response measurement: rotor impact

Measurement of impact-related transient vibration is considered important for the potential to detect rotor rub/contact events. The use of rotor-mounted accelerometers may hold advantages in

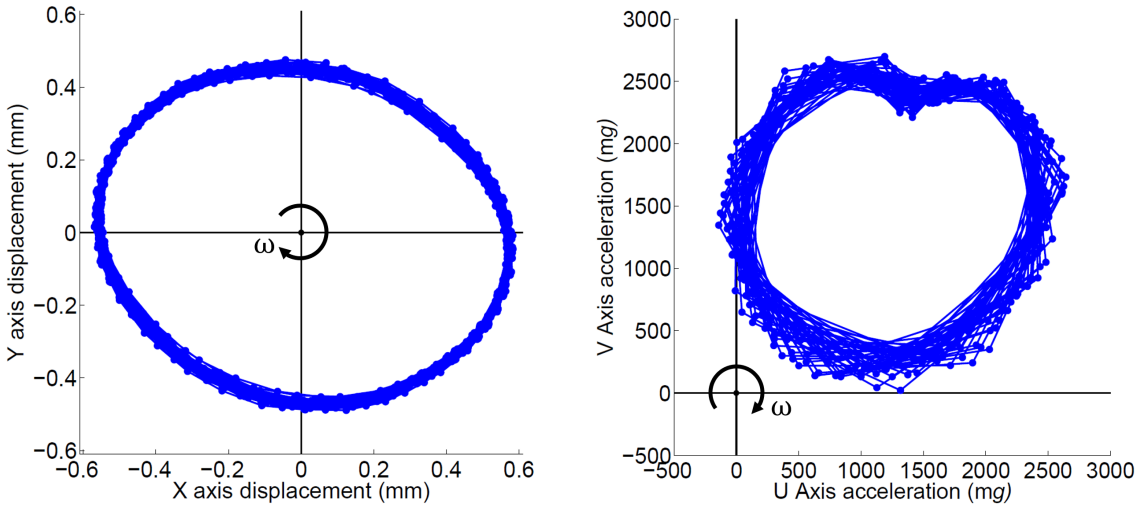

(a) Inertial reference frame (b) Accelerometer output

Figure 13: Rotor orbit at 2,000 rpm measured with stator-mounted displacement sensors and rotor-mounted accelerometers.

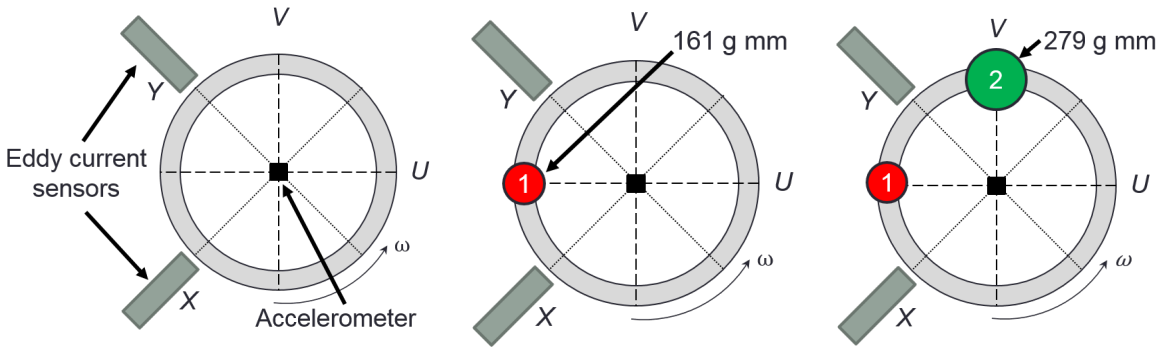

(a) Unbalance condition 1 (b) Unbalance condition 2 (c) Unbalance condition 3

Figure 14: Tested unbalance conditions with added masses 1 and 2.

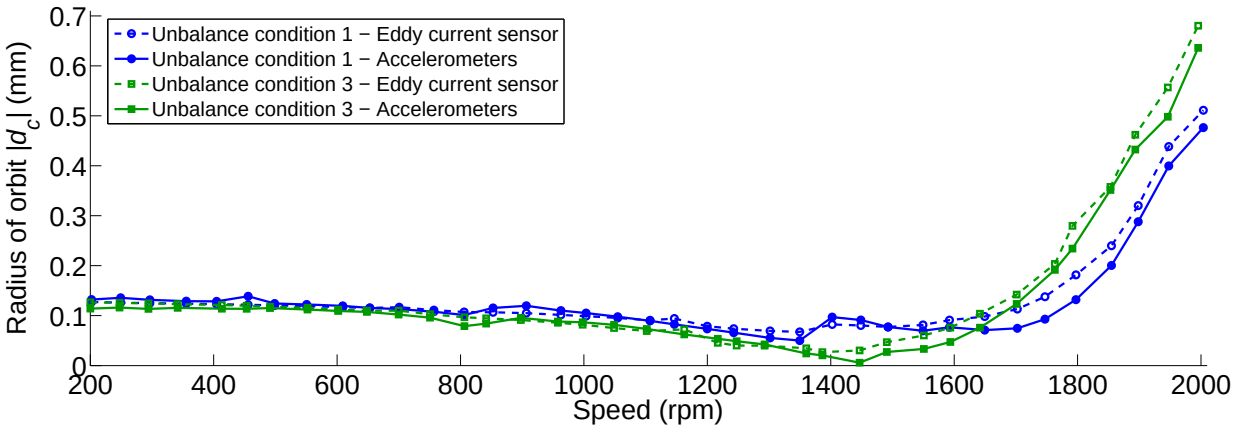

Figure 15: Accelerometer and eddy current sensor displacement data for Unbalance conditions 1 and 3.

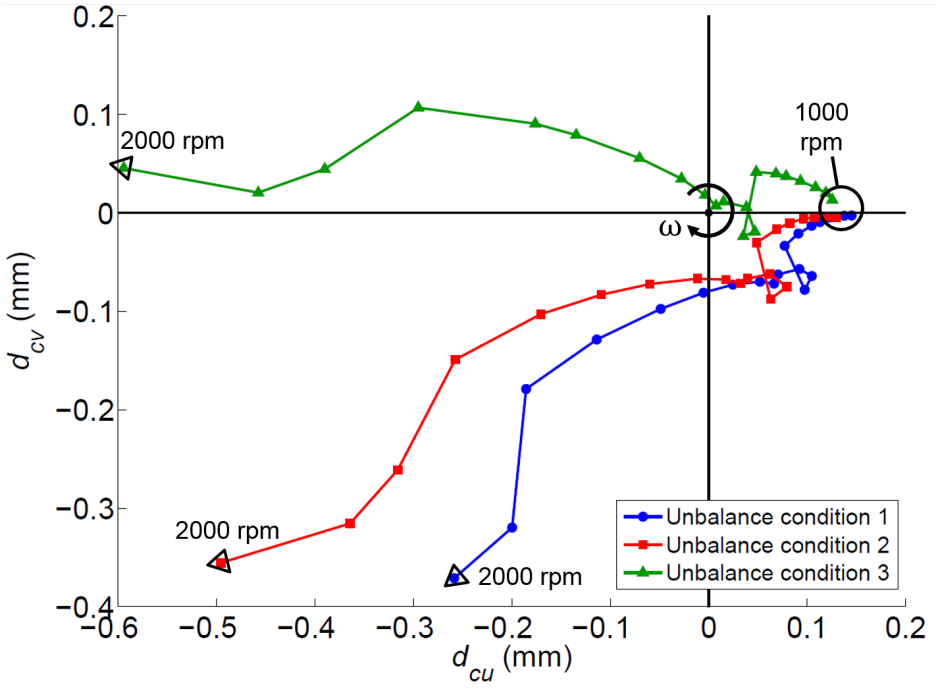

Figure 16: Rotor d_c Measurements for the three unbalance conditions.

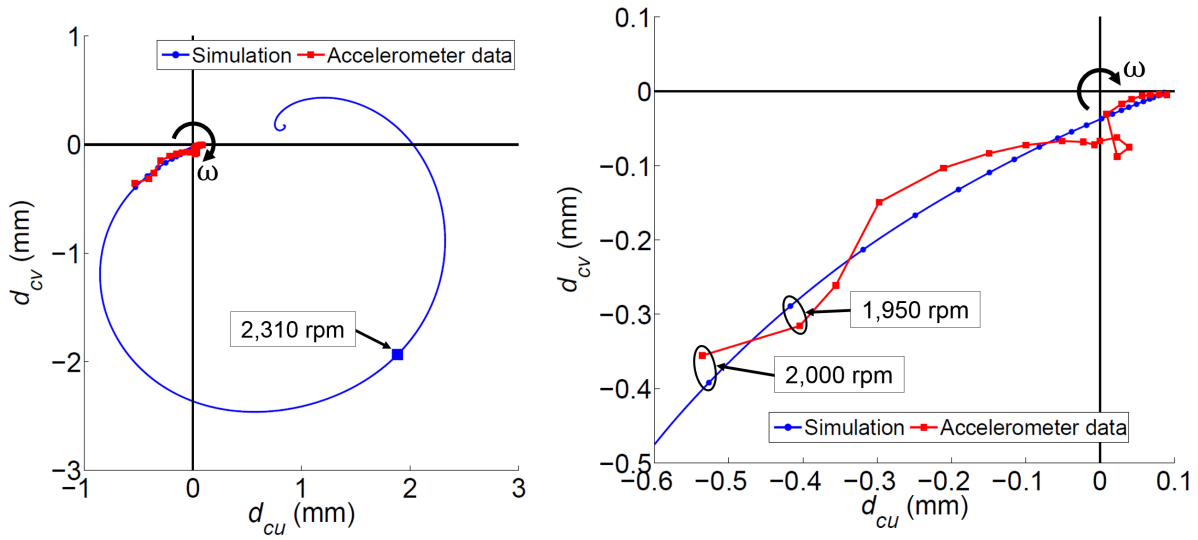

(a) Up to 2,500 rpm

(b) Detailed view up to 2,000 rpm

Figure 17: Comparison between experimental d_c displacement data and model-based predictions. The critical speed (2,310 rpm) is labeled.

detecting vibration locally and with improved sensitivity to high frequency components compared to displacement measurements.

An impulsive force will give rise to non-synchronous transient components in the rotor orbit. It can be modelled as a time-delayed half sine function, such that

$$F_I(t) = \begin{cases} 0 & \text{if } t < T \\ F_0 \sin \omega_p (t - T) & \text{if } T \leq t \leq \frac{\pi}{\omega_p} + T \\ 0 & \text{if } t > \frac{\pi}{\omega_p} + T \end{cases} \tag{39}$$

where $\frac{\pi}{\omega_p}$ is the duration of the pulse and F_0 is its amplitude. For a force input of the form $\mathbf{u} = F_I(t)\boldsymbol{\beta}$ where $\boldsymbol{\beta} = [0, 0, \ldots, \cos\beta_i, \sin\beta_i, \ldots, 0, 0]^{\mathrm{T}}_{(2n\times 1)}$ is a vector indicating the coordinate and angle of incidence β_i of the force,

$$\int_0^t \mathrm{e}^{\lambda_m(t-\tau)}\mathbf{u}(\tau)\,\mathrm{d}\tau = \begin{cases} 0 & \text{if } t < T \\ \boldsymbol{\beta}\frac{F_0}{(\lambda_m^2+\omega_p^2)}\left(-\lambda_m \sin\omega_p(t-T) - \omega_p\cos\omega_p(t-T) + \omega_p \mathrm{e}^{\lambda_m(t-T)}\right) & \text{if } T \leq t \leq \frac{\pi}{\omega_p} + T \\ \boldsymbol{\beta}\frac{F_0\omega_p}{(\lambda_m^2+\omega_p^2)}\left(1 + \mathrm{e}^{-\lambda_m\frac{\pi}{\omega_p}}\right)\mathrm{e}^{\lambda_m(t-T)} & \text{if } t > \frac{\pi}{\omega_p} + T \end{cases} \tag{40}$$

If the pulse duration is assumed to be small, only the response beyond $t = \frac{\pi}{\omega_p} + T$ will be of practical interest. Hence, the rotor displacement in response to an impact occurring at time T will be

$$d_{xy}(t) = F_0 \sum_{m=-4n}^{4n} (v_{rm} + \mathrm{j}v_{sm})\hat{\mathbf{b}}_m^{\mathrm{T}}\boldsymbol{\beta}\frac{\omega_p}{(\lambda_m^2+\omega_p^2)}\left(1 + \mathrm{e}^{-\lambda_m\frac{\pi}{\omega_p}}\right)\mathrm{e}^{\lambda_m(t-T)} \tag{41}$$

Consequently,

$$a_m(t) = \mathrm{j}g\mathrm{e}^{-\mathrm{j}\omega t} + F_0 \sum_{m=-4n}^{4n} (v_{rm} + \mathrm{j}v_{sm})\hat{\mathbf{b}}_m^{\mathrm{T}}\boldsymbol{\beta}\frac{\lambda_m^2\omega_p}{(\lambda_m^2+\omega_p^2)}\left(1 + \mathrm{e}^{-\lambda_m\frac{\pi}{\omega_p}}\right)\mathrm{e}^{[(\lambda_m - \mathrm{j}\omega)t - \lambda_m T]} \tag{42}$$

The conjugate pair of system eigenvalues associated with a particular vibration mode will take the form $\lambda_m = -\alpha_m + \mathrm{j}\omega_m$ and $\lambda_{-m} = -\alpha_m - \mathrm{j}\omega_m$, where α_m is the modal decay term and ω_m is the damped natural frequency. Hence, the displacement for an unbalanced rotor after a single impulse applied to the rotor mid-plane, considering only the dominant first modal response, will be

$$d_{xy} = R_{F\sigma}\mathrm{e}^{\mathrm{j}(\omega t + \phi_{F\sigma})} + R_{B\sigma}\mathrm{e}^{\mathrm{j}(-\omega t + \phi_{B\sigma})} + A_1\mathrm{e}^{(-\alpha_1 + \mathrm{j}\omega_1)t} + A_{-1}\mathrm{e}^{(-\alpha_1 - \mathrm{j}\omega_1)t} \tag{43}$$

where, for clarity, the constant amplitude terms are grouped as

$$A_1 = F_0(v_{r1} + \mathrm{j}v_{s1})\hat{\mathbf{b}}_1^{\mathrm{T}}\boldsymbol{\beta}\frac{\omega_p}{(\lambda_1^2+\omega_p^2)}\left(1 + \mathrm{e}^{-\lambda_1\frac{\pi}{\omega_p}}\right)\mathrm{e}^{-\lambda_1 T}$$

$$A_{-1} = F_0(v_{r-1} + \mathrm{j}v_{s-1})\hat{\mathbf{b}}_{-1}^{\mathrm{T}}\boldsymbol{\beta}\frac{\omega_p}{(\lambda_{-1}^2+\omega_p^2)}\left(1 + \mathrm{e}^{-\lambda_{-1}\frac{\pi}{\omega_p}}\right)\mathrm{e}^{-\lambda_{-1} T}$$

It follows that the accelerometer output will be

$$a_m = -\omega^2 R_{F\sigma} \mathrm{e}^{\mathrm{j}\phi_{F\sigma}} - \omega^2 R_{B\sigma} \mathrm{e}^{\mathrm{j}(-2\omega t + \phi_{B\sigma})} + \mathrm{j}g\mathrm{e}^{-\mathrm{j}\omega t} + \lambda_1^2 A_1 \mathrm{e}^{(-\alpha_1 + \mathrm{j}(\omega_1 - \omega))t} + \lambda_{-1}^2 A_{-1} \mathrm{e}^{(-\alpha_1 - \mathrm{j}(\omega_1 + \omega))t} \tag{44}$$

Therefore, the transient vibration components measured by the internal accelerometers will have frequencies $\omega_m - \omega$ and $-(\omega_m + \omega)$.

A series of impact tests were carried out to confirm the capability of the internal accelerometers to accurately detect transient vibration of the rotor shaft. The rotor was operated at steady speeds of 0, 400, 800, 1,200 and 1,600 rpm. For each case an impulse was applied to the rotor using an impact hammer while measurements were recorded with both the accelerometers and the eddy current displacement sensors.

The analytical description of the rotor response in Eq. (44) is confirmed by comparing the Fourier Transform of the response measured by both the eddy current and internal accelerometer sensors at 1,600 rpm in Fig. 18. For the stator-mounted sensors the main amplitude peaks correspond to the operating speed ω (26.7 Hz), its higher harmonic 2ω (53.3 Hz) and the resonant frequency ω_r (38.5 Hz). In the case of the internally mounted accelerometers those peaks are found at ω due to the gravitational acceleration term, 2ω due to the non-circular orbit described by the rotor and also at $\omega_r - \omega$ (12 Hz) and $\omega_r + \omega$ (65 Hz), which are produced by the hammer strike.

Irrespective of the source, vibration data can be transformed between the inertial and rotating reference frames following Eq. (6). Figure 19 shows rotor acceleration in the rotating frame of reference following an impact at 400 rpm. The internal accelerometer signals are compared with acceleration data reconstructed from the eddy current sensor displacement measurements. The impact occurs at approximately 14.75 seconds, and the transient vibrations decay within approximately half a second. Both data show similar response behaviour, demonstrating that the internal accelerometers can capture transient vibration behaviour in the same way as conventional eddy current displacement sensors.

6.3. Rotational speed measurement

The accelerometer signals exhibit a component due to gravity that is independent of vibration and depends only on the angle of rotation (Eq. (6)). Because of this, it can be used as a reference to the inertial frame, which allows tracking of rotational speed.

In theory, the spectral analysis of the accelerometer signals should produce a gravity component with a magnitude of 1 g at the synchronous frequency. However, sampled data may suffer from spectral leakage, whereby the energy of a particular spectral component is spread between adjacent frequency bins [20]. A FFT-based algorithm was developed to track the 1 g amplitude peak such that an accurate value for average rotational speed of the rotor could be obtained:

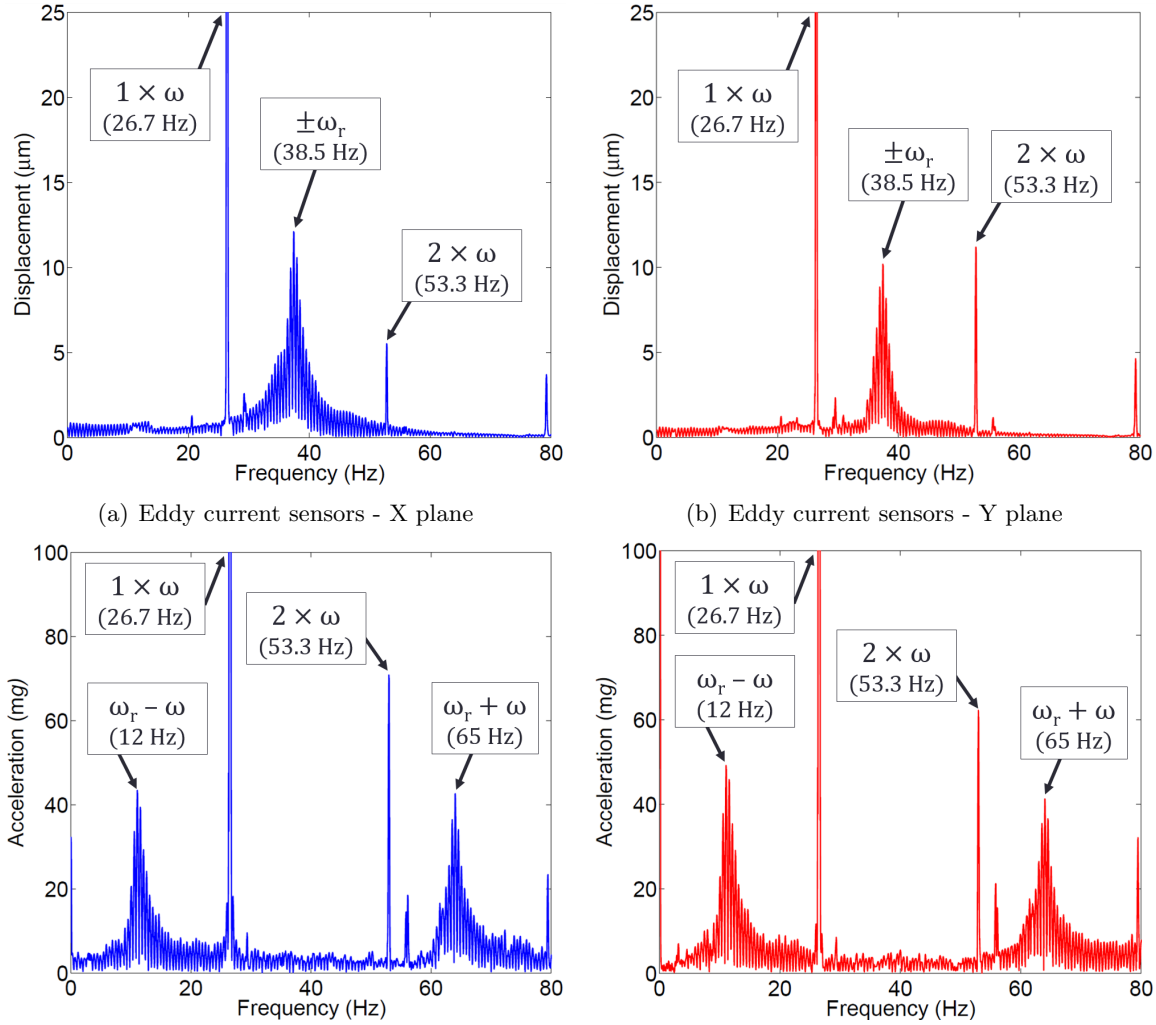

(a) Eddy current sensors - X plane

(b) Eddy current sensors - Y plane

(c) Accelerometers - U plane

(d) Accelerometers - V plane

Figure 18: FFT of sensor data collected during impulsive impact tests with rotor operating at 1,600 rpm.

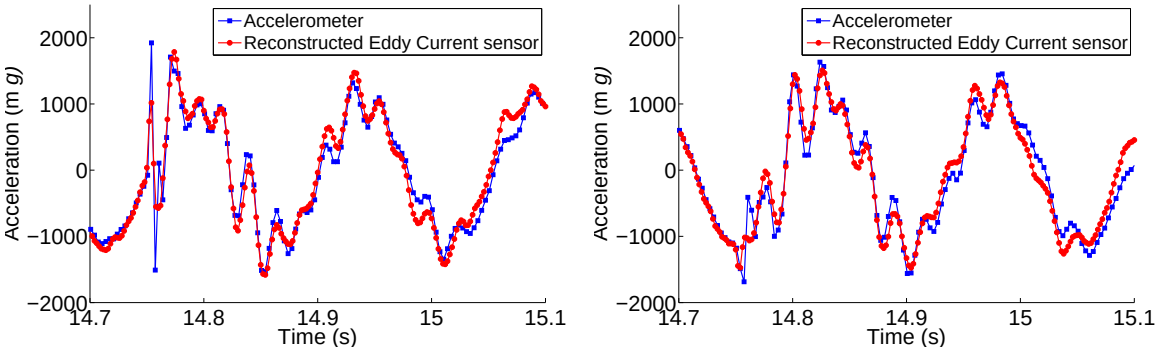

(a) U axis

(b) V axis

Figure 19: Transient vibration as measured by accelerometers and reconstructed from eddy current sensor data.

Table 4: Flat top window coefficients.

Coefficient	q_0	q_1	q_2	q_3	q_4
Value	1	1.932	1.286	0.388	0.032

1. Perform a FFT over a short time interval of the accelerometer data using a flat top window function.
2. Find local maxima and mark those with a magnitude greater than 900 mg as feasible synchronous frequencies.
3. Identify which of the feasible frequencies corresponds to the rotating speed of the rotor.
4. Repeat steps 1-3 with the rectangular window, using the information gleaned with the flat top window to guide the identification.
5. Refine the speed estimation by using a frequency domain interpolation method [21].

To ensure identification of the 1 g amplitude component, a window function is initially used to modify the FFT spectrum of the accelerometer signal, a_m. A rectangular window function occurs naturally when sampling and produces the best frequency resolution, but has large amplitude errors [22]. Because of this, a flat top window is used, which is designed to have the lowest amplitude measurement error:

$$w(n) = q_0 - q_1 \cos\left(\frac{2\pi n}{N-1}\right) + q_2 \cos\left(\frac{4\pi n}{N-1}\right) - q_3 \cos\left(\frac{6\pi n}{N-1}\right) + q_4 \cos\left(\frac{8\pi n}{N-1}\right) \tag{45}$$

where N is the number of samples of a_m used in the FFT and $0 \leq n \leq N-1$. The q_i coefficients are given in Table 4 [20]. The identification of the synchronous frequency in step 3 can be achieved by selecting the frequency which is closest to the previous estimated speed or establishing a maximum deviation criteria which eliminates any candidate frequencies falling outside of a feasible speed variation range. For more complex vibration cases the historical FFT data can be used to discard candidate frequencies which appear in prior speed estimations, under the assumption that they must correspond to other types of vibration phenomena.

The frequency resolution of this technique is directly related to the window size:

$$R_f = \frac{f_s}{W} \tag{46}$$

where R_f is the frequency resolution, f_s is the sampling frequency and W is the window size in number of samples. Larger window sizes will give improved frequency resolution at the expense of increased delay in speed estimation and are more suitable for rotors operating under quasi steady state conditions. In cases where the rotor speed may change rapidly, window sizes must be kept short.

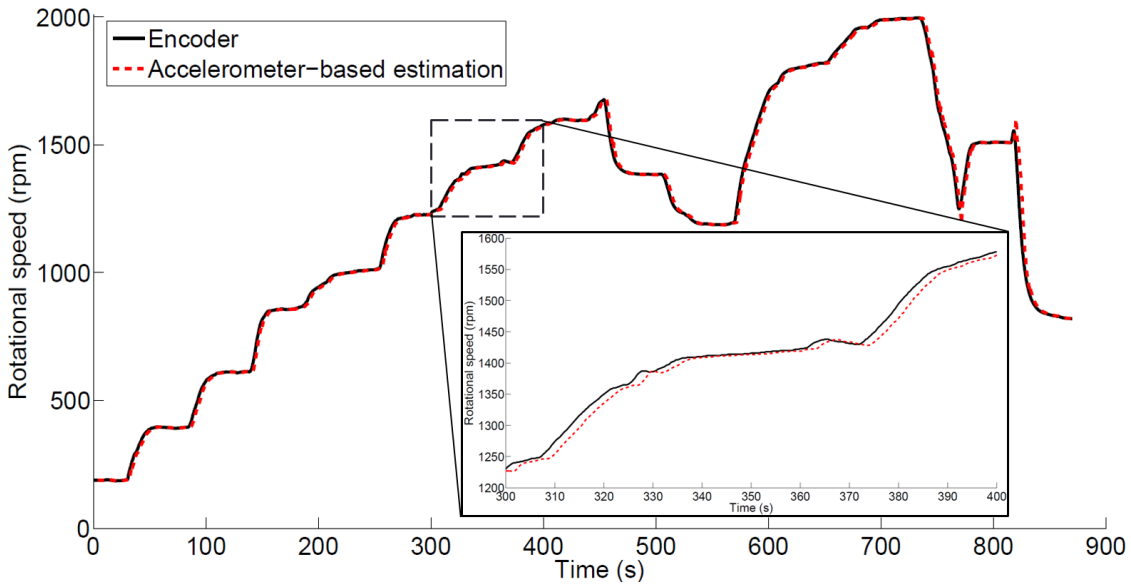

Figure 20: Estimated rotor speed using accelerometer-based virtual encoder compared against encoder-measured data.

6.3.1. Rotor speed estimation results

The speed estimation algorithm was tested on a rotor operating at a range of speeds between 200 and 2,000 rpm. The test included constant speed intervals of approximately 30 seconds as well as acceleration and deceleration.

A comparison between the speed estimated using the accelerometers and the speed measured by the encoder is presented in Fig. 20. The data are shown for a sampling rate of 300 Hz and a window size of 1,200 samples (4 second window size). The detailed view of the results shows how the estimation is delayed due to the fact that data is recorded over the time interval before processing. The use of the accelerometer signals as a virtual encoder provides good real-time estimation of the rotor speed within 15 rpm (the frequency resolution) of the true speed even during acceleration and deceleration.

7. Conclusions

A new theoretical framework for the use of rotor-mounted accelerometers to measure absolute steady and transient vibratory motion of a rotor has been introduced. The validity of the approach has been demonstrated by examining and comparing analytical and experimental results. An analysis of error sources shows that zero-g and positional offsets require calibration prior to operating the rotor, and techniques to mitigate them have been demonstrated.

The novel topology was applied to detect steady state rotor response associated with unbalance. The results were validated by comparing the obtained vibration results against eddy current

displacement measurements. It has been shown that both the magnitude and phase information of the response can be obtained directly from accelerometer data, without requiring timing marks. Impact response measurements were used to study accelerometer-based sensing of transient vibration, with results demonstrating the equivalence between internal accelerometer measurements and conventional eddy current sensor data. Differences in the spectral components of both types of sensor signal can be directly related to the transformation between inertial and rotating reference frames.

The use of internal accelerometers to provide rotational speed measurement has also been demonstrated, introducing a technique based on tracking the gravitational component in the acceleration frequency spectrum. The method employed is robust and can be applied to horizontal rotors irrespective of the state of vibration and during acceleration and deceleration.

Acknowledgments

The authors are grateful to the EPSRC for supporting this research through studentship award 1223129.

References

[1] A. W. Lees, Smart machines with flexible rotors, Mechanical Systems and Signal Processing 25 (1) (2011) 373–382.

[2] E. H. Maslen, G. Schweitzer, Magnetic Bearings: Theory, Design, and Application to Rotating Machinery, Springer, 2009.

[3] J. Van de Vegte, Continuous automatic balancing of rotating systems, Journal of Mechanical Engineering Science 6 (3) (1964) 264–269.

[4] Z. Gosiewski, Automatic balancing of flexible rotors, part i: Theoretical background, Journal of Sound and Vibration 100 (4) (1985) 551–567.

[5] C.-W. Lee, Y.-D. Kim, Modal balancing of flexible rotors during operation: Design and manual operation of balancing head, Proceedings of the Institution of Mechanical Engineers, Part C: Journal of Mechanical Engineering Science 201 (5) (1987) 349–355.

[6] S. W. Dyer, J. Ni, Adaptive influence coefficient control of single-plane active balancing systems for rotating machinery, Journal of Manufacturing Science and Engineering 123 (2) (2000) 291–298. doi:10.1115/1.1349554.

[7] Z. Gosiewski, Automatic balancing of flexible rotors, part ii: Synthesis of system, Journal of Sound and Vibration 114 (1) (1987) 103–119.

[8] C.-W. Lee, Y.-D. Joh, Y.-D. Kim, Automatic modal balancing of flexible rotors during operation: Computer controlled balancing head, Proceedings of the Institution of Mechanical Engineers, Part C: Journal of Mechanical Engineering Science 204 (1) (1990) 19–28.

[9] S. W. Dyer, J. Shi, J. Ni, K.-K. Shin, Robust optimal influence-coefficient control of multiple-plane active rotor balancing systems, Journal of Dynamic Systems, Measurement, and Control 124 (1) (2002) 41–46.

[10] H.-G. Horst, H. P. Wolfel, Active vibration control of a high speed rotor using pzt patches on the shaft surface, Journal of Intelligent Material Systems and Structures 15 (9-10) (2004) 721–728.

[11] R. Christensen, I. Santos, Active rotor-blade control vibration using shaft-based electro-magnetic actuation, Journal of Engineering for Gas Turbines and Power 128 (3) (2006) 644–652.

[12] D. Knappett, J. Garcia, Blade tip timing and strain gauge correlation on compressor blades, Proceedings of the Institution of Mechanical Engineers, Part G: Journal of Aerospace Engineering 222 (4) (2008) 497–506.

[13] P. Sloetjes, A. de Boer, Vibration reduction and power generation with piezoceramic sheets mounted to a flexible shaft, Journal of Intelligent Material Systems and Structures 19 (1) (2008) 25–34.

[14] L. Arebi, F. Gu, A. Ball, Rotor misalignment detection using a wireless sensor and a shaft encoder, in: Future Technologies in Computing and Engineering. Proceedings of Computing and Engineering Annual Researchers' Conference CEARC'10, Huddersfield, UK, 2010, pp. 6–13.
[15] L. Arebi, F. Gu, A. Ball, A comparative study of misalignment detection using a novel wireless sensor with conventional wired sensors, in: Journal of Physics: Conference Series, Vol. 364, IOP Publishing, 2012, p. 012049.
[16] L. Baghli, J. F. Pautex, S. Mezani, Wireless instantaneous torque measurement, application to induction motors, in: 19th International Conference on Electrical Machines, ICEM, Rome Italy, 2010.
[17] M. Elnady, J. Sinha, S. Oyadiji, Identification of critical speeds of rotating machines using on-shaft wireless vibration measurement, in: Journal of Physics: Conference Series, Vol. 364, IOP Publishing, 2012, p. 012142.
[18] M. Elnady, A. Abdelbary, J. Sinha, S. Oyadiji, Fe and experimental modeling of on-shaft vibration measurement, in: 15th International Conference on Aerospace Sciences & Aviation Technology, Cairo, Egypt, 2013, pp. 1–18.
[19] S. Han, Measuring displacement signal with an accelerometer, Journal of Mechanical Science and Technology 24 (6) (2010) 1329–1335.
[20] G. D'Antona, Digital Signal Processing for Measurement Systems. Theory and Applications, New York : Springer-Verlag, 2006.
[21] A. Ferrero, S. Salicone, S. Toscani, A fast, simplified frequency-domain interpolation method for the evaluation of the frequency and amplitude of spectral components, Instrumentation and Measurement, IEEE Transactions on 60 (5) (2011) 1579–1587.
[22] F. J. Harris, On the use of windows for harmonic analysis with the discrete fourier transform, Proceedings of the IEEE 66 (1) (1978) 51–83.